ACS APPLIED MATERIALS & INTERFACES
Research Article
www.acsami.org

Visible-Light Photochemical Activity of Heterostructured Core–Shell Materials Composed of Selected Ternary Titanates and Ferrites Coated by TiO_2

Li Li,[†] Xuan Liu,[†] Yiling Zhang,[†] Noel T. Nuhfer,[†] Katayun Barmak,[‡] Paul A. Salvador,[†] and Gregory S. Rohrer*,[†]

[†]Department of Materials Science and Engineering, Carnegie Mellon University, Pittsburgh, Pennsylvania 15213, United States
[‡]Department of Applied Physics and Applied Mathematics, Columbia University, New York, New York 10027, United States

ABSTRACT: Heterostructured photocatalysts comprised of microcrystalline (mc-) cores and nanostructured (ns-) shells were prepared by the sol–gel method. The ability of titania-coated $ATiO_3$ (A = Fe, Pb) and $AFeO_3$ (A = Bi, La, Y) catalysts to degrade methylene blue in visible light ($\lambda > 420$ nm) was compared. The catalysts with the titanate cores had enhanced photocatalytic activities for methylene blue degradation compared to their components alone, whereas the catalysts with ferrite cores did not. The temperature at which the ns-titania shell is crystallized influences the photocatalytic dye degradation. mc-$FeTiO_3$/ns-TiO_2 annealed at 500 °C shows the highest reaction rate. Fe-doped TiO_2, which absorbs visible light, did not show enhanced photocatalytic activity for methylene blue degradation. This result indicates that iron contamination is not a decisive factor in the reduced reactivity of the titania coated ferrite catalysts. The higher reactivity of materials with the titanate cores suggests that photogenerated charge carriers are more easily transported across the titanate–titanate interface than the ferrite–titanate interface and this provides guidance for materials selection in composite catalyst design.

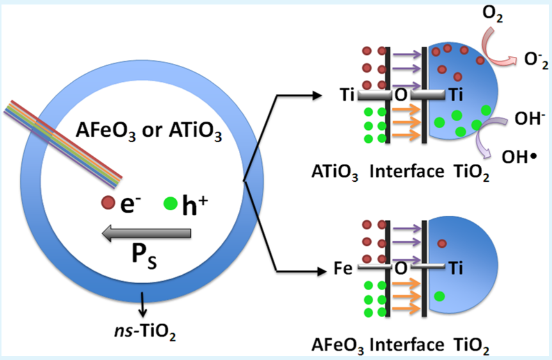

KEYWORDS: *core–shell, photocatalyst, TiO_2, dye degradation, ferrite, titanate*

1. INTRODUCTION

TiO_2 is one of the most widely studied photocatalysts because of its appropriate electronic structure, photostability, chemical inertness, and commercial availability.[1−7] Titania's photochemical efficiency in visible light is limited by several factors, such as the recombination of photogenerated charge carriers, the back reaction of intermediates, insufficient active sites for the redox reactions, and especially its wide band gap. Various methods have been used to modify TiO_2 to make it more active under visible light, such as metal and nonmetal doping,[3,8−12] dye sensitization,[13,14] the formation of junctions with other semiconductors,[15,16] and coupling to narrow band gap semiconductors.[17−24] For example, CdS,[25] Cu_2O,[26] BiOI,[22] $ZnFe_2O_4$,[27] and $CuInS_2$,[28] were combined with TiO_2 for visible-light sensitization and the heterostructured materials showed enhanced reactivity for organic pollutant degradation and hydrogen production.

The combination of titania with different semiconductors is potentially promising because heterostructured photocatalysts can combine multiple functionalities within a single structure.[24,29] Among different configurations for heterostructured photocatalysts, the core/shell structure has been widely investigated as a means to enhance light absorption, charge transfer, and surface area.[30,31] Several heterostructured catalysts comprised of micocrystalline, visible light absorbing cores ($FeTiO_3$ and $PbTiO_3$), coated by nanostructured titania, have recently been shown to have enhanced visible light photochemical reactivity.[32,33] These materials combine the high surface area that is necessary to provide enough active sites for high reactivity with the good crystallinity required to transport photogenerated carriers without recombination.[34] Finally, the addition of an internal field within the light absorbing core separates photogenerated charge carriers and thus decreases recombination. This internal field can arise from different sources, such as ferroelectric spontaneous polarization,[35−37] or polar surface terminations.[38,39] For example, a $BaTiO_3$/TiO_2 core/shell heterstructure shows enhanced photocatalytic hydrogen production compared to its components alone.[40]

On the basis of the success of $FeTiO_3$/TiO_2, $PbTiO_3$/TiO_2, and $BaTiO_3$/TiO_2 heterostructured catalysts with microcrystalline cores and nanocrystalline shells, it is reasonable to hypothesize that cores with narrower gaps will absorb more visible light and be more reactive. The purpose of this paper is to test this hypothesis. In general, ferrites have narrower bandgaps than titanates, so we will compare the photochemical activities of heterostructured catalysts with Fe containing cores

Received: March 10, 2013
Accepted: May 6, 2013
Published: May 6, 2013

dx.doi.org/10.1021/am4008837 | *ACS Appl. Mater. Interfaces* 2013, 5, 5064−5071

to those with Ti containing cores. Specifically, ABO_3 cores with Fe on the B site ($BiFeO_3$, $LaFeO_3$, $YFeO_3$) and with Ti on the B site ($FeTiO_3$, $PbTiO_3$) were coated by TiO_2, and their abilities to degrade methylene blue were compared. In each compound, the B cation is octahedarally coordinated by oxygen. Note also the Fe in $FeTiO_3$ is divalent and is on the A-site, so it is considered a titanate; in the ferrites, the Bi, Y, and La cations are on the A-site and are trivalent. All of the compounds have perovskite-related structures, except $FeTiO_3$, which has the illmenite structure. This collection of core materials includes some that are ferroelectric ($PbTiO_3$, $BiFeO_3$) and some that are not ($LaFeO_3$, $YFeO_3$, $FeTiO_3$), as well n-type and p-type materials. In all the heterostructures, the cores selectively absorb the light used to promote the reaction, which is too low in energy to promote excitation in the titania shell. The enhanced reactivity of the composites with titanate cores compared to the ferrite cores suggests that the transfer of charge from the core to the shell is less efficient in the ferrite/titanate heterostructures.

2. EXPERIMENTAL SECTION

Core Materials Preparation. $PbTiO_3$ (99.9%, Alfa Aesar) and $FeTiO_3$ (99.8%, Alfa Aesar) micrometer-sized powders were obtained from commercial sources. (Bi, La, Y)FeO_3 microcrystals were produced using methods described below. $BiFeO_3$ was prepared using a modification of a previously reported hydrothermal method.[41] Equal amounts of 0.005 mol bismuth nitrate pentahydrate ($Bi(NO_3)_3{\cdot}5H_2O$, Acros Organics, 98%) and iron nitrate nonahydrate ($Fe(NO_3)_3{\cdot}9H_2O$, Acros Organics, 99+%) were used as the starting materials and dissolved into 50 mL of a 0.5 M dilute nitric acid (HNO_3, Acros Organics, 68%) solution with magnetic stirring at 70 °C for 30 min. After complete dissolution, a 9 M potassium hydroxide (KOH, Acros Organics, 85.3%) solution was added dropwise into the solution above with constant stirring to coprecipitate $Bi(OH)_3$ and $Fe(OH)_3$. The pH of the final solution was adjusted to be 14. The resulting brown precipitate was filtered and washed several times using distilled water to remove K^+, OH^-, and NO_3^- ions. Next, 50 mL of KOH was mixed with the precipitate in a 100 mL beaker. Potassium nitrate (KNO_3, Acros Organics, 99+%) was added into the mixture as a comineralizer to control the growth of the powders. The suspension was stirred and dispersed at room temperature for 20 min and then transferred to a 125 mL acid digestion vessel with Teflon PFA inner walls (Parr Instrument Company). The vessel was kept at 180 °C for different durations under auto generated pressures (related to the temperature and amount of water). After natural cooling to room temperature, the products were collected and washed with distilled water by centrifugation for several times to remove the residual K^+, OH^-, and NO_3^- ions. Finally, the product was dried at 80 °C for 5 h.

$LaFeO_3$ microcrystals were produced using the EDTA-initiated sol−gel method.[42] 1.4 mol of EDTA ($C_{10}H_{16}N_2O_8$, Acros Organics, 99%) per mole of metal was dissolved into water at ambient temperature. 45 mL ammonia (NH_3OH, Fisher Scientific, 29.04%) was added dropwise, as slowly as possible, into the EDTA solution to keep the pH around 7. 0.03 mol lanthanum nitrate hexahydrate ($La(NO_3)_3{\cdot}6H_2O$, Acros Organics, 99.999%) and iron nitrate nonahydrate were mixed with the EDTA/ammonia solution. During this process, precipitation was avoided. The mixture was heated at 60 °C for 3 h and then transferred to a drying oven for 2 days to form the black gel. The gel was then ground into powder and calcined at 600 °C (at a heating rate of 10 °C/min) for 24 h to burn off the organic component. The calcined powder was then annealed at 900 °C for 24 h (heated at 10 °C/min) for crystallization. The final product was collected after grinding the calcined powders.

$YFeO_3$ was synthesized using a method similar to that used for $LaFeO_3$. $YFeO_3$ was fabricated using a sol−gel method with citric acid as a linking reagent. 0.03 mol yttrium nitrate hexahydrate ($Y(NO_3)_3{\cdot}6H_2O$, Acros Organics, 99%) and iron nitrate nonahydrate ($Fe(NO_3)_3{\cdot}9H_2O$, Acros Organics, 99%+) were dissolved into 100 mL of a 0.72 mol/L citric acid ($C_6H_8O_7$, Acros Organics, 99.5%) solution; 26.5 mL ammonia was then slowly added to the mixture. The pH of the solution was neutral and stirred for 3 h at 60 °C. The solution was then dried at 130 °C for 2 days to form a xerogel. The xerogel was then calcined and sintered in exactly the same way as the $LaFeO_3$.

ABO_3/TiO_2 Heterostructure Preparation. ABO_3 microcrystals were coated with TiO_2 using the sol−gel method by the hydrolysis of TBOT ($Ti(OC_4H_9)_4$, Acros Organics, 99.0%).[40] The ABO_3 microcrystals were suspended in 29 mL of ethanol/water (20 mL/9 mL) solution and sonicated for 30 min. Ten milliliters of acetic acid was added to adjust the pH. Another solution was prepared with a suitable amount (15 mL) of ethanol, 8.6 mL of TBOT, and 1 mL of 2,4-pentanedione. The transparent TBOT solution was added dropwise to the ABO_3 suspension with stirring for 2 h. The mixture was then aged at 90 °C in a water bath for 24 h. The xerogel collected from the mixture was ground and then calcined at 500 °C for 2 h with 5 °C/min heating rate to obtain the final product. $FeTiO_3/TiO_2$ heterostructures were sintered at temperatures between 400 and 600 °C to investigate the influence of annealing temperature.

TiO_2 nanoparticles were obtained from the same procedure, but without the addition of the ABO_3 core materials. Several control samples were also prepared. Fe-doped TiO_2 was produced by adding 1 mol % $Fe(NO_3)_3{\cdot}9H_2O$ into the precursor and otherwise adhering to the TiO_2 preparation described above. Physical mixtures of $FeTiO_3$ and TiO_2 were made by combining them with the mass ratio of 1:2 in ethanol and sonicating them at 80 °C for 3 h. The mixtures were then dried at 70 °C for 12 h.

Characterization. The phase composition was investigated by X-ray diffraction (XRD) using a diffractometer (PANalytical, X'Pert Pro, Philips) equipped with a CuK_α radiation source and operated at 45 kV and 40 mA. Diffraction patterns were collected from 10° to 90° at a scanning rate of 3°/min and a step size of 0.05° for all θ-2θ scans. Transmission electron microscopy (TEM, Tecnai F20), with an accelerating voltage of 200 kV, was used to characterize the morphology of the heterostructured photocatalyst. The TEM sample was prepared by dispersing the powder ultrasonically in methanol for 10 min and then distributing several drops of the suspension into a 200 mesh copper grid coated with a carbon support film. The reflectance spectra of the samples were recorded by a UV−vis spectrometer (Ocean Optics USB2000) equipped with a R600−7 reflection probe optimized for the 250−800 nm region. The Brunauer−Emmett−Teller (BET) surface area was measured by nitrogen adsorption/desorption isothermal measurement (Nova 2200e, Quantachrome, FL) at 77 K. The sample was vacuum-degassed for 3 h at 300 °C to reduce the moisture before measurement.

Methylene Blue Degradation. Methylene blue (MB) photocatalytic degradation was used to evaluate the photocatalytic properties of the powders. The dye degradation experiment was performed at room temperature in a 100 mL quartz photochemical reactor. An aqueous suspension of 0.3 g photocatalyst was added into 65 mL of 1×10^{-5} M MB solution. Prior to irradiation, the suspension was stirred in the dark for 2 h to achieve absorption/desorption equilibrium between the photocatalyst and the dye. The photocatalytic reaction was initiated by irradiating the reaction system with a 300 W high-pressure mercury lamp for 5 h. A UV cutoff filter (Oriel, $\lambda > 420$ nm) with 20 cm^2 window was placed between the quartz reactor and the lamp to cut off the UV light. Five milliliters of dye solution was taken each hour and then centrifuged to remove the particulate photocatalyst before measuring the UV−vis absorption spectrum. The initial absorbance intensity of the solution at 663.89 nm (the characteristic absorption peak of methylene blue) was denoted as C_0. The ratio between the absorbance intensity of the sample after photocatalytic reaction and C_0 is used to evaluate the degradation of methylene blue.

3. RESULTS

XRD patterns of mc-$FeTiO_3$/ns-TiO_2 heterostructures and their components are shown in Figure 1a. All diffraction peaks from the heterostructures and the corresponding component

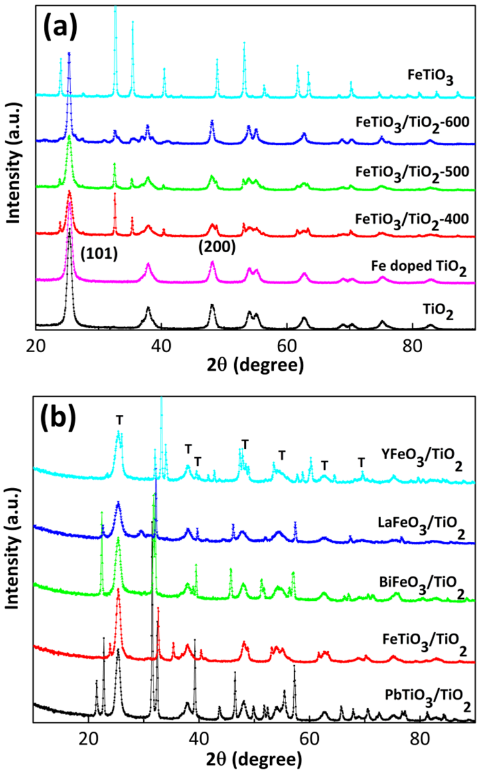

Figure 1. X-ray diffraction pattern of (a) mc-$FeTiO_3$/ns-TiO_2 core/shell heterostructures, annealed at different temperatures from 400 to 600 °C, and their components; (b) mc-ferrites/ns-TiO_2 and mc-titanates/ns-TiO_2 annealed at 500 °C. The diffraction pattern of 1 mol % Fe doped TiO_2 is also shown. The number after the heterostructure represents annealing temperature in the preparation of the heterostructure (e.g., −400 indicates annealing at 400 °C). The peak relating to TiO_2 was also marked with "T" in the uppermost diffraction pattern in b.

ferrites or titanates can be indexed to the standard diffraction pattern of anatase TiO_2 (JCPDS 46−1237) and $FeTiO_3$ (JCPDS 75−1211). The observation of anatase is consistent with previous reports that indicate the conversion temperature from anatase to rutile occurs at temperatures greater than 600 °C.[43,44] That no other phases were observed implies no reaction occurs between $FeTiO_3$ and TiO_2 at these temperatures. With an increase of the annealing temperature from 400 to 600 °C, the width of the peak at 25.28°, which is related to (101) plane of anatase TiO_2, narrows. This result can be explained if the crystal size of the nanostructured TiO_2 coating increased with the increase of annealing temperature, as a result of the thermal coarsening.

Figure 1b shows the phase composition of heterostructured powders annealed at 500 °C. The titania phases are designated by the "T" and marked above the corresponding peaks. No secondary phases were observed in those powders; all peaks could be indexed to TiO_2 and the corresponding ferrites or titanates components (anatase TiO_2, JCPDS 46−1237; $PbTiO_3$, JCPDS 06−0452; $FeTiO_3$, JCPDS 75−1211; $BiFeO_3$, JCPDS 86−1518; $LaFeO_3$, JCPDS 37−1493; and $YFeO_3$, JCPDS 39−1489). No reaction is observed between the component phases. TiO_2 peaks marked in the figure are primarily anatase.

Though no unexpected phases were observed in the heterostructures, it is possible that some Fe diffusion into the TiO_2 occurred, as reported in similar heterostructures.[45] For comparison with the potentially Fe-doped titania coatings, we prepared unsupported 1 mol % Fe-doped TiO_2. The TiO_2 phase in the doped TiO_2 powder was also anatase. The (101) and (200) diffraction peaks, respectively at 25.28° and 48.05°, were used to calculate the *a* and *c* lattice parameters of tetragonal anatase, as well as the unit-cell volumes. Table 1 presents the comparison of lattice parameters for undoped TiO_2, Fe-doped TiO_2 and TiO_2 in the mc-$FeTiO_3$/ns-TiO_2 heterostructure. The Fe-doped TiO_2 had no difference in the *a* lattice parameter, but the *c* parameter decreased as did the unit-cell volume. This indicates the addition of Fe^{3+} leads to the shrinkage of the unit cell along the *c* axis. Considering that the ionic radius of Fe^{3+} (0.64 Å) is a little smaller than Ti^{4+} (0.68 Å),[46] it is reasonable that Ti^{4+} can be substituted by Fe^{3+} at low concentrations causing only a small decrease in the unit-cell volume. The lattice parameters and unit cell volume of TiO_2 in $FeTiO_3$/TiO_2 heterostructures is similar to that of undoped TiO_2. This indicates little Fe diffuses from the $FeTiO_3$ core to the TiO_2 shell.

Table 1. Lattice Parameters of TiO_2, Fe-Doped TiO_2 (D-TiO_2), and TiO_2 in the Heterostructure (H-TiO_2)

materials	d_{101}(Å)	d_{200}(Å)	*a* (Å)	*c* (Å)	*V* (Å)
TiO_2	3.501	1.889	3.778	9.315	133.0
D-TiO_2	3.493	1.889	3.778	9.167	130.8
H-TiO_2	3.507	1.893	3.786	9.308	133.4

The core−shell microstructure and morphology of mc-$BiFeO_3$/ns-TiO_2 heterostructured powders annealed at 500 °C was analyzed in detail using TEM. A low-magnification TEM bright-field image that includes an entire particle is shown in Figure 2a. The dark region is assumed to be the $BiFeO_3$ microcrystalline core, surrounded by a semitransparent layer

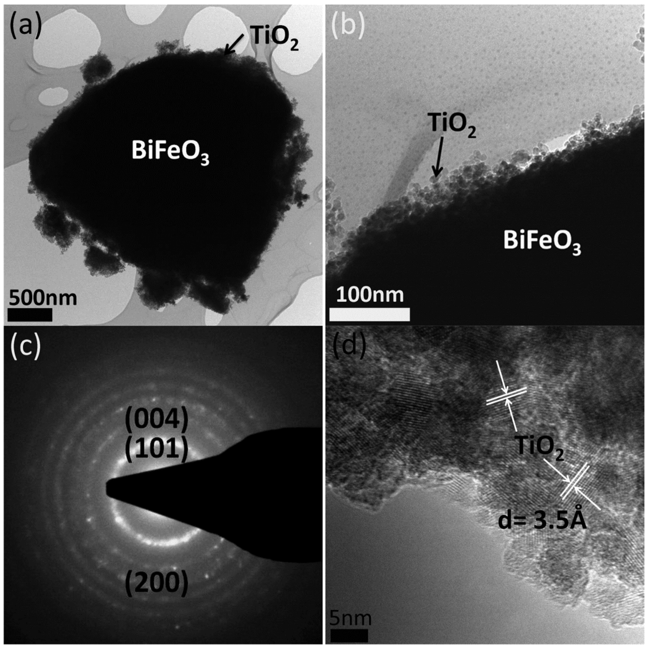

Figure 2. TEM images of mc-$BiFeO_3$/ns-TiO_2 heterostructured powders annealed at 500 °C. (a) Low-magnification bright-field images of an entire particle, (b) high-magnification bright-field image of detail around the $BiFeO_3$ and TiO_2 interface, (c) SAED of TiO_2 coating, (d) HRTEM image of TiO_2 coating.

that is assumed to be the nanostructured TiO_2 shell. A higher-magnification bright-field TEM image, taken from the semi-transparent region, is shown in Figure 2b. In this figure, the transparent layer is clearly composed of TiO_2 nanoparticles with approximate diameters of 10−15 nm. This is consistent with the 9 nm particle diameter value calculated using the measured width of the TiO_2 XRD peak and the Scherrer equation. A sharp and clear interface can be observed between mc-$BiFeO_3$ core and ns-TiO_2 shell. The observations of $BiFeO_3/TiO_2$ are characteristic of the other core−shell materials and examples can be found in earlier publications.[32,33,40]

The selected area electron diffraction pattern (SAED) of the TiO_2 nanostructured coating is shown in Figure 2c. The SAED result is a ring pattern, rather than bright sharp dots, because of the polycrystalline nature of the nanostructured TiO_2 coatings. Those diffraction circles were indexed and identified as the planes of tetragonal anatase TiO_2. Figure 2d is the high-resolution TEM (HRTEM) image of TiO_2 coating. The atomic arrangement is highlighted with the white solid line. The distance between two contiguous atomic planes is measured to be 3.5 Å, which is consistent with the value of interplanar distance of the (101) planes in anatase TiO_2. These results are consistent with earlier results on heterostructured catalysts with titanate cores.[32]

The optical properties of mc-$FeTiO_3$/ns-TiO_2 heterostructures annealed at different temperatures and their components are shown in Figure 3a. $FeTiO_3$ shows strong absorption both in the UV and visible light range. The reported band gap energy of $FeTiO_3$ varies widely in the literature, but the value for bulk $FeTiO_3$ is generally reported to be between 2.5 and 2.6 eV.[47−50] Values as high as 3.55 eV have also been reported for a $FeTiO_3$ thin film.[51] The absence of a peak or edge in the UV−vis spectrum of $FeTiO_3$ relating to the bandgap excitation is explained by absorption from the intervalence charge transfer between Fe^{2+} and Ti^{4+} (and Fe^{3+} and Ti^{3+}) that occurs at a lower energy.[32,50]

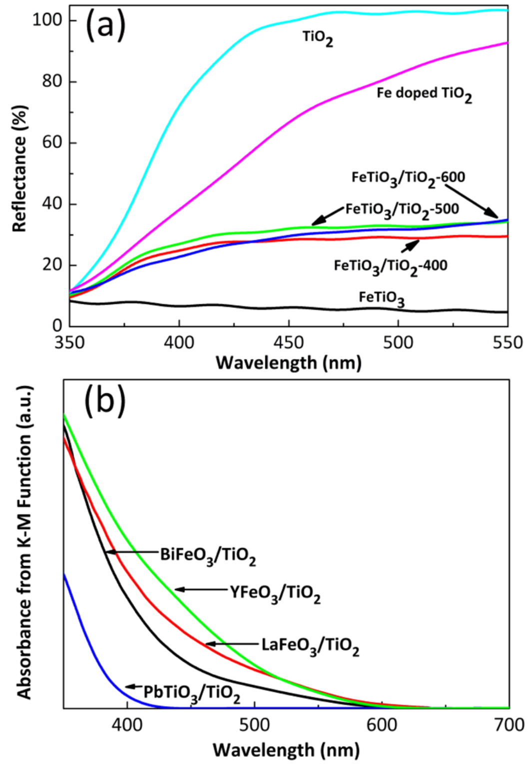

Figure 3. UV−visible spectra of (a) mc-$FeTiO_3$/ns-TiO_2 heterostructures annealed at different temperatures, its components, and Fe-doped TiO_2 and (b) $PbTiO_3/TiO_2$ as well as the ferrite/TiO_2 heterostructures annealed at 500 °C.

The heterostructured powders annealed at different temperatures show similar reflectance to each other in the UV and visible range. No significant difference for light absorption is observed. In addition, the reflectance of the heterostructured powders is more similar to $FeTiO_3$ than TiO_2. Combined with the XRD result that little Fe doping is observed in the TiO_2 coating, the similarity of the optical properties of mc-$FeTiO_3$/ns-TiO_2 heterostructures to $FeTiO_3$ indicates the mc-$FeTiO_3$ core is the primary light absorbing component in the heterostructure (though absorption in the coating cannot be ruled out). The Fe-doped TiO_2 powder (which is yellow in color) extends its absorption edge into the deep visible-light range and shows stronger absorption in both the UV and visible range than the undoped sample. The UV−visible absorption of $PbTiO_3/TiO_2$ and (Bi, La, Y)FeO_3/TiO_2 is shown in Figure 3b. The (Bi, La, Y)FeO_3/TiO_2 heterostructures showed stronger visible-light absorption than the materials with titanate cores and absorbed light with wavelengths less than about 590 nm.

The physical properties of $FeTiO_3/TiO_2$ annealed at different temperatures and their reactivities for photocatalytic dye degradation of methylene blue are shown in Table 2, compared to the single phases of each material. The surface area of $FeTiO_3$ is 0.47 m^2/g, indicating the powder is in the micrometer-size range. The surface area of mc-$FeTiO_3$/ns-TiO_2 decreases from 93 m^2/g at 400 °C to 40 m^2/g at 600 °C. The pore volume of mc-$FeTiO_3$/ns-TiO_2 annealed at 600 °C is smaller than for samples annealed at 400 and 500 °C, indicating that the titania has densified.

Table 2. Physical Properties of Heterostructured Powders and Their Reaction Rates for the Photocatalytic Degradation of Methylene Blue (K_{MB})

catalyst	processing temp (°C)	BET surface area (m^2/g)	pore vol (cc/g)	K_{MB} (h^{-1})
TiO_2	500	83	0.14	0.05
$FeTiO_3$	500	0.47	0.003	0.03
$FeTiO_3/TiO_2$	400	93	0.13	0.04
	500	73	0.11	0.17
	600	40	0.06	0.09

Figure 4 shows methylene blue degradation under visible light irradiation when catalyzed by $FeTiO_3/TiO_2$ annealed at 500 °C. (It should be noted that no dye degradation was observed without the addition of a photocatalyst). The time evolution of dye degradation, represented as C/C_0, is consistent the pseudo first-order kinetic model for the reaction.[44,50,52,53] The mc-$FeTiO_3$/ns-TiO_2 heterostructure exhibits high visible-light photocatalytic reactivity when compared with its components, both in the degradation rate, which is represented as the slope of $\ln(C_0/C)$ vs time, and the amount of dye degraded after 6 h. The reaction rates, K_{MB}, of mc-$FeTiO_3$/ns-TiO_2 and its components are shown in Table 2. The MB removal rate of mc-$FeTiO_3$/ns-TiO_2 (0.17 h^{-1}) is 3.4 times that of TiO_2 (0.05 h^{-1}) and 5.7 times that of $FeTiO_3$ (0.03 h^{-1}), respectively. The corresponding reactivity of a mechanical mixture of $FeTiO_3$ and TiO_2 (0.03 h^{-1}) is only about 18% of

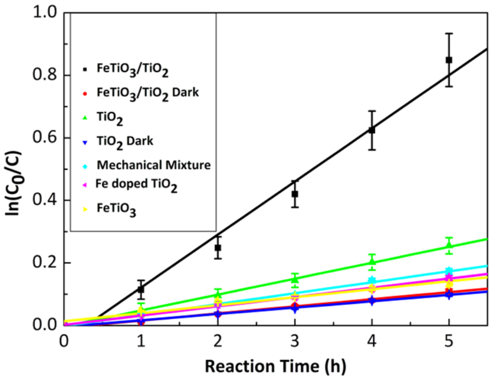

Figure 4. Photodegradation of methylene blue with $FeTiO_3/TiO_2$ annealed at 500 °C and its components. The reactivity of a $FeTiO_3$ and TiO_2 mechanical mixture as well as Fe-doped TiO_2 are also shown.

the core/shell structure, which demonstrates that the core/shell heterostructured powder is more active. In addition, the reactivity of mc-$FeTiO_3$/ns-TiO_2 and TiO_2 for methylene blue dye degradation in the dark is also presented in Figure 4. Little degradation was observed for the powders without irradiation, which confirms that the photocatalyst is stable in such conditions.

TiO_2 exhibits higher dye degradation rates under visible-light illumination than in the dark, even though it does not absorb visible light. This phenomenon is known as "TiO_2-mediated dye degradation" or "self-photosensitized degradation" of dyes.[54,55] In this process, TiO_2 is not excited to produce electrons and holes but only provides the pathway to transfer the injected electrons from the excited dye to an adsorbed dye molecule on the TiO_2 surface for degradation.

To test if the enhancement of the photocatalytic activity for mc-$FeTiO_3$/ns-TiO_2 originates from the interdiffusion of Fe to the TiO_2 coating, Fe-doped TiO_2 was prepared and tested for MB degradation under visible light. The previous literature reports that Fe doping can extend the absorption of TiO_2 to the visible-light range, which was also observed in our UV−vis experiments.[56] This has been suggested to arise from the creation of a donor level above the valence band edge; the donor level leads to absorption in the visible region, and thus, leads to photocatalytic activity enhancement for water splitting and some dye degradation experiments.[57,58] However, the substituted Fe dopants can also serve as centers for charge carrier recombination,[59,60] which then reduces the overall photocatalytic activity. The current experiments demonstrate that 1% Fe doping did not enhance the photocatalytic activity of TiO_2 for MB degradation and implies that unintentional Fe doping of TiO_2 is not likely the cause of the high reactivity of mc-$FeTiO_3$/ns-TiO_2 heterostructured powders.

The influence of annealing temperature on the photocatalytic activity of heterostructured powders is shown in Table 2. mc-$FeTiO_3$/ns-TiO_2 annealed at 500 °C exhibits the highest reactivity for MB degradation among the three samples. The reactivity of the sample annealed at 500 °C ($0.17\ h^{-1}$) is 4.3 times and 1.9 times that of the powders annealed at 400 °C ($0.04\ h^{-1}$) and 600 °C ($0.09\ h^{-1}$), respectively. It is noteworthy that the sample annealed at 500 °C is more reactive than the one annealed at 400 °C, even though it has a smaller surface area. These collected observations will be discussed further, after first presenting the results from the perovskite iron-oxides ($AFeO_3$).

The physical properties of $AFeO_3/TiO_2$ (A = Bi, La, Y) and $PbTiO_3/TiO_2$ are listed in Table 3. Compared to TiO_2 annealed at 500 °C, (Pb, Fe)TiO_3/TiO_2 shows low surface area, whereas (Bi, La, Y)FeO_3/TiO_2 displays high surface area. This phenomenon can be explained by a difference in the scaffold effect from the core to the microstructure of the nanostructured coating. Organic molecules are removed from the three-dimensional network of the xerogel during annealing and interparticle pores were formed. This is the origin of porosity of the nanostructured coating. The pore structure then begins to collapse with a further increase of temperature. The core can scaffold the pore structure, preventing the coating from collapsing to some degree and coating densification is decreased. In this case, (Bi, La, Y)FeO_3 cores resist coating densification better than (Pb, Fe)TiO_3 cores. The large pore volumes for (Bi, La, Y)FeO_3/TiO_2 support this view.

Table 3. Physical Properties of Heterostructured Powders and Their Reaction Rates for the Photocatalytic Degradation of Methylene blue (K_{MB})

catalyst	processing temp (°C)	BET surface area (m^2/g)	pore vol (cc/g)	K_{MB} (h^{-1})
$PbTiO_3/TiO_2$	500	74	0.15	0.24
$BiFeO_3/TiO_2$	500	104	0.20	0.07
$LaFeO_3/TiO_2$	500	109	0.23	0.04
$YFeO_3/TiO_2$	500	115	0.22	0.01

The visible-light reactivities of the photocatalysts synthesized for this work, measured by using the degradation of methylene blue, are shown in Figure 5 and listed in Table 3. The compounds with Fe on the B-site show less photocatalytic activity for dye degradation than those with Ti on the B-site. Although mc-$BiFeO_3$/ns-TiO_2 shows a slightly higher degradation rate than TiO_2 alone, mc-$LaFeO_3$/ns-TiO_2 and mc-$YFeO_3$/ns-TiO_2 have an even lower reactivity. All of the single component powders (*mc*-$PbTiO_3$, mc-$FeTiO_3$, mc-$BiFeO_3$, mc-$LaFeO_3$, and mc-$YFeO_3$) show little reactivity for methylene blue degradation. Their reactivities are far smaller than TiO_2 alone because of their small surface areas. This result also means the enhanced reactivity of some of the heterostructured

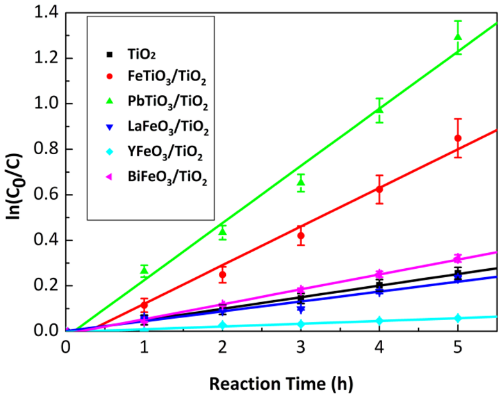

Figure 5. Photodegradation of methylene blue with (Pb, Fe)TiO_3/TiO_2 and (Bi, La, Y)FeO_3 annealed at 500 °C and TiO_2 under visible light illumination.

powders originates from the interaction between core and shell, rather than the components alone.

4. DISCUSSION

The primary observation in this paper is that $ATiO_3/TiO_2$ (A = Pb,Fe) shows significantly enhanced photocatalytic activity under visible light irradiation when compared to their components alone, while $AFeO_3/TiO_2$ (A = Bi, La, Y) does not. This interesting phenomenon suggests that the B site in ABO_3/TiO_2 is directly related to the photocatalytic activity of the heterostructures. There are several possible mechanisms for the enhanced reactivity of the titanate systems in comparison to the ferrites: the positions of the band edges, internal polarizations, built in potentials from differences in the majority carrier type, continuity of bonding across the interface, and carrier density. Each of these possibilities is discussed briefly below.

The band edge positions of various core materials and TiO_2 are listed in Table 4. The conduction band positions of TiO_2 and $FeTiO_3$ have been measured.[32,61] The flat band conduction band positions (E_c) of the other materials are estimated using the method proposed by Butler and Ginley.[62] It should be noted that these estimates have uncertainties of at least 100 mV.

Table 4. Electronic Properties of Various Core Materials and TiO_2 (E_{bg} is the Band Gap Energy, E_a is the Electron Affinity, E_c is the Conduction Band Position, and E_v is the Valence Band Position)

materials	E_{bg} (eV)	E_a (eV)	E_c (eV)	E_v (eV)
$PbTiO_3$	2.85	4.23	−0.27	2.58
$FeTiO_3$	2.6[32]	4.6	0.1	2.7
$BiFeO_3$	2.1	4.85	0.35	2.45
$LaFeO_3$	2.1	4.5	0	2.1
$YFeO_3$	2.1	4.6	0.1	2.2
TiO_2	3.2	4.1	−0.4	2.8

Figure 6 compares the estimated band positions of the materials considered here relative to standard hydrogen electrode (SHE) level, which is defined as 0 eV. According to these estimates, all of the conduction band edges are below that of TiO_2 and they do not differ in energy by more than 620 mV. There is no obvious trend between the band edge positions and the reactivities of the heterostructures. In fact, there are no significant differences between the band edge positions of the compounds with Fe and Ti on the B-sites. The only notable correlation is that the compounds containing Fe on the B-site all have valence band edge positions that are above the positions of the titanates. This suggests that a larger hole transfer overpotential at the ferrite/titanate might limit the reactivity of the ferrite based materials.

It has previously been shown that the ferroelectrics can have enhanced photochemical response.[33,40] The internal field from the micrometer-sized ferroelectric cores can assist in the separation of photogenerated electrons and holes and thus improve the efficiency of the ferroelectric/TiO_2 heterostructures. Therefore, the compounds studied here were selected so that there would be ferroelectric and nonferroelectic examples of both the titanates and ferrites. Although the ferroelectric examples ($PbTiO_3$ and $BiFeO_3$) of each composition type degraded methylene blue faster than the nonferroelectric examples, the nonferroelectric titanate was better than all of the ferrites. Furthermore, $BiFeO_3$ supported titania is not significantly better than unsupported titania. On the basis of these findings, the ferroelectric properties by themselves cannot explain the trends in the photochemical reactivity of these heterostructures.

The presence of a p−n junction at the interface between the core and the titania coating will create and internal field that can separate photogenerated charge carriers and this will potentially increase the reactivity. Titania is n-type in all normal situations. However, both $PbTiO_3$ (n-type) and $FeTiO_3$ (p-type) have enhanced reactivities. The ferrites are all p-type and will form n-p junctions with titania, yet do not have enhanced reactivity. On this basis, the presence or absence of a p−n junction does not appear to be a dominant factor determining the relative reactivity of these compounds.

A final possible reason for the enhanced activity of the titanates is the continuity of Ti−O−Ti bonds across the $ATiO_3/TiO_3$ interface. This might reduce the barrier for transmission across the interface from where the carriers are generated (the core) to where they react with the solution (the titania shell). Both the Ti and Fe are octahedrally coordinated in the core (Fe and Ti) and shell (Ti). The bonding between Fe^{3+} in the FeO_6 octahedra to Ti^{4+} in TiO_6 octahedra will form Fe−O−Ti bonds, which changes the polarity compared to Ti−O−Ti interfacial bonds.[63] It is reasonable to assume that electrons occupying states in bands formed by the overlap of Ti and O orbitals will experience less of a potential change at the interface than electrons in states formed from the overlap of a Fe and O orbital, and thus experience less scattering. It should be noted that the pore volume and surface area of $AFeO_3/TiO_2$ are larger than those of $ATiO_3/TiO_2$ (Tables 2 and 3). The

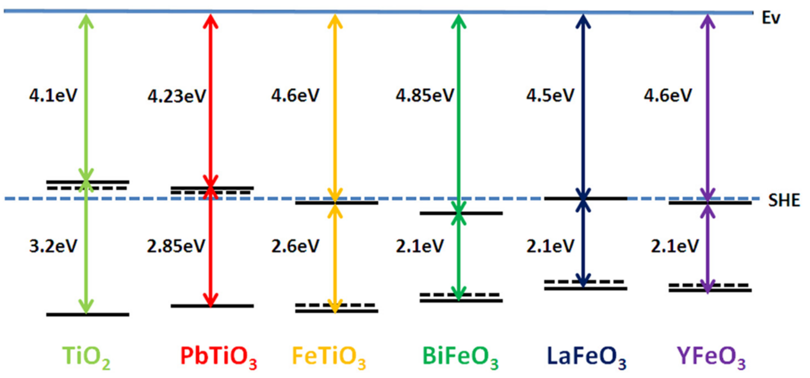

Figure 6. Schematic of band gap and band energy levels for the materials considered here.

denser coatings in the latter system may be the result of stronger bonding between $ATiO_3$ and TiO_2 than between $AFeO_3$ and TiO_2. The enhancement of reactivity of mc-$FeTiO_3$/ns-TiO_2 for methylene blue degradation with increased annealing temperature suggests that the interface quality and bonding between the core and shell are beneficial for the improvement of photocatalytic activity. Finally, it must also be noted that the structure of $FeTiO_3$ differs from the perovskite cores used in this study. $FeTiO_3$ takes the ilmenite structure and is made up of both FeO_6 and TiO_6 octahedra.[50] Though both Fe^{3+}/Ti^{3+} and Fe^{2+}/Ti^{4+} pairs exist in $FeTiO_3$, $FeTiO_3$ still can be considered as one member of a series of compounds that includes the titanates $A^{2+}Ti^{4+}O_3$ and there will still be Ti−O−Ti bonds at the core−shell interface.[50,64,65]

The idea that continuous metal−oxygen−metal bonds across the phase boundary promotes charge transfer is consistent with results from polymorphs of TiO_2 and Ga_2O_3. Bickley et al. suggested that the high reactivity of P25 titainia is the result of absorption in an anatase core and then charge transfer to a thin rutile overlayer.[15] Similarly, Wang et al. ascribed the high photocatalytic activity of α-/β-Ga_2O_3 composites to charge transfer between the two polymorphs.[16] These past findings, together with the present results, suggest that when selecting materials to form a composite catalyst based on a semiconductor junction, both phases should have the same metal−oxygen bonds on either side of the interface.

One last physical characteristic of the materials that could affect reactivity is the charge carrier density, which was not controlled or quantified in these experiments. If the relatively high reactivity in the titanates derives from a space charge region at the interface between the two phases that separates charges and reduces recombination, then the width of this region would vary with the carrier density. So, if the ferrites systematically have a much higher concentration of carriers than the titanates, then these carriers would more effectively screen the charge at the core−shell interface, reducing the volume of the material in the space charge region where recombination is suppressed. This would lead to reduced reactivity in the materials with higher charge carrier density.

■ CONCLUSION

$PbTiO_3/TiO_2$ and $FeTiO_3/TiO_2$ heterostructures showed enhanced photocatalytic activities compared to their components while $BiFeO_3/TiO_2$, $LaFeO_3/TiO_2$, and $YFeO_3/TiO_2$ did not. The observation that catalysts with titanate cores showed enhanced reactivity while catalysts with ferrite cores did not is not simply correlated to energy level positions, built in potentials, or the presence of dipolar fields from ferroelectrics. The continuity of bonding at the interface between the titanate core and the titania shell is the most likely explanation for the enhanced reactivity found in $PbTiO_3/TiO_2$ and $FeTiO_3/TiO_2$.

■ AUTHOR INFORMATION

Corresponding Author

*E-mail: gr20@andrew.cmu.edu. Fax: 412-268-7596. Tel: 412-268-2696.

Notes

The authors declare no competing financial interest.

■ ACKNOWLEDGMENTS

This work was supported by National Science Foundation Grant DMR 1206656 and the PA DCED.

■ REFERENCES

(1) Chen, X.; Liu, L.; Yu, P. Y.; Mao, S. S. *Science* **2011**, *331*, 746−750.

(2) Fujishima, A.; Honda, K. *Nature* **1972**, *238*, 37−38.

(3) Asahi, R.; Morikawa, T.; Ohwaki, T.; Aoki, K.; Taga, Y. *Science* **2001**, *293*, 269−271.

(4) Leung, D. Y. C.; Fu, X. L.; Wang, C. F.; Ni, M.; Leung, M. K. H.; Wang, X. X.; Fu, X. Z. *Chemsuschem* **2010**, *3*, 681−694.

(5) Hernandez-Alonso, M. D.; Fresno, F.; Suarez, S.; Coronado, J. M. *Energy Environ. Sci.* **2009**, *2*, 1231−1257.

(6) Hashimoto, K.; Irie, H.; Fujishima, A. *Jpn. J. Appl. Phys.* **2005**, *44*, 8269−8285.

(7) Hu, X.; Li, G.; Yu, J. C. *Langmuir* **2009**, *26*, 3031−3039.

(8) Choi, J.; Park, H.; Hoffmann, M. R. *J. Phys. Chem. C* **2010**, *114*, 783−792.

(9) Braun, A.; Akurati, K. K.; Fortunato, G.; Reifler, F. A.; Ritter, A.; Harvey, A. S.; Vital, A.; Graule, T. *J. Phys. Chem. C* **2010**, *114*, 516−519.

(10) Ren, W. J.; Ai, Z. H.; Jia, F. L.; Zhang, L. Z.; Fan, X. X.; Zou, Z. G. *Appl. Catal. B: Environ.* **2007**, *69*, 138−144.

(11) Wang, X. H.; Li, J. G.; Kamiyama, H.; Moriyoshi, Y.; Ishigaki, T. *J. Phys. Chem. B* **2006**, *110*, 6804−6809.

(12) Xu, H.; Zhang, L. Z. *J. Phys. Chem. C* **2010**, *114*, 940−946.

(13) Kiwi, J.; Borgarello, E.; Pelizzetti, E.; Visca, M.; Grätzel, M. *Angew. Chem., Int. Ed. Engl.* **1980**, *19*, 646−648.

(14) Borgarello, E.; Kiwi, J.; Pelizzetti, E.; Visca, M.; Gratzel, M. *Nature* **1981**, *289*, 158−160.

(15) Bickley, R. I.; Gonzalez-Carreno, T.; Lees, J. S.; Palmisano, L.; Tilley, R. J. D. *J. Solid State Chem.* **1991**, *92*, 178−190.

(16) Wang, X.; Xu, Q.; Li, M.; Shen, S.; Wang, X.; Wang, Y.; Feng, Z.; Shi, J.; Han, H.; Li, C. *Angew. Chem., Int. Ed.* **2012**, *51*, 13089−13092.

(17) Jang, J. S.; Li, W.; Oh, S. H.; Lee, J. S. *Chem. Phys. Lett.* **2006**, *425*, 278−282.

(18) Jang, J. S.; Ji, S. M.; Bae, S. W.; Son, H. C.; Lee, J. S. *J. Photochem. Photobiol. A: Chem.* **2007**, *188*, 112−119.

(19) Jang, J. S.; Choi, S. H.; Kim, H. G.; Lee, J. S. *J. Phys. Chem. C* **2008**, *112*, 17200−17205.

(20) Cao, T. P.; Li, Y. J.; Wang, C. H.; Shao, C. L.; Liu, Y. C. *Langmuir* **2011**, *27*, 2946−2952.

(21) Zhong, J.; Chen, F.; Zhang, J. L. *J. Phys. Chem. C* **2010**, *114*, 933−939.

(22) Zhang, X.; Zhang, L.; Xie, T.; Wang, D. *J. Phys. Chem. C* **2009**, *113*, 7371−7378.

(23) Huang, H. J.; Li, D. Z.; Lin, Q.; Shao, Y.; Chen, W.; Hu, Y.; Chen, Y. B.; Fu, X. Z. *J. Phys. Chem. C* **2009**, *113*, 14264−14269.

(24) Huang, H.; Li, D.; Lin, Q.; Zhang, W.; Shao, Y.; Chen, Y.; Sun, M.; Fu, X. *Environ. Sci. Technol.* **2009**, *43*, 4164−4168.

(25) Li, G.; Wu, L.; Li, F.; Xu, P.; Zhang, D.; Li, H. *Nanoscale* **2013**, *5*, 2118−2125.

(26) Lalitha, K.; Sadanandam, G.; Kumari, V. D.; Subrahmanyam, M.; Sreedhar, B.; Hebalkar, N. Y. *J. Phys. Chem. C* **2010**, *114*, 22181−22189.

(27) Hou, Y.; Li, X.; Zhao, Q.; Quan, X.; Chen, G. *Environ. Sci. Technol.* **2010**, *44*, 5098−5103.

(28) Shen, F.; Que, W.; Liao, Y.; Yin, X. *Ind. Eng. Chem. Res.* **2011**, *50*, 9131−9137.

(29) Maeda, K.; Domen, K. *J. Phys. Chem. Lett.* **2010**, *1*, 2655−2661.

(30) Elder, S. H.; Cot, F. M.; Su, Y.; Heald, S. M.; Tyryshkin, A. M.; Bowman, M. K.; Gao, Y.; Joly, A. G.; Balmer, M. L.; Kolwaite, A. C.; Magrini, K. A.; Blake, D. M. *J. Am. Chem. Soc.* **2000**, *122*, 5138−5146.

(31) Hirakawa, T.; Kamat, P. V. *J. Am. Chem. Soc.* **2005**, *127*, 3928−3934.

(32) Gao, B.; Kim, Y. J.; Chakraborty, A. K.; Lee, W. I. *Appl. Catal. B* **2008**, *83*, 202−207.

(33) Li, L.; Zhang, Y.; Schultz, A. M.; Liu, X.; Salvador, P. A.; Rohrer, G. S. *Catal. Sci. Technol.* **2012**, *2*, 1945−1952.

(34) Kudo, A.; Miseki, Y. *Chem. Soc. Rev.* **2009**, *38*, 253−278.

(35) Burbure, N. V.; Salvador, P. A.; Rohrer, G. S. *Chem. Mater.* **2010**, *22*, 5823−5830.

(36) Burbure, N. V.; Salvador, P. A.; Rohrer, G. S. *Chem. Mater.* **2010**, *22*, 5831−5837.

(37) Tiwari, D.; Dunn, S. *J. Mater. Sci.* **2009**, *44*, 5063−5079.

(38) Giocondi, J. L.; Rohrer, G. S. *J. Am. Ceram. Soc.* **2003**, *86*, 1182−1189.

(39) Schultz, A. M.; Salvador, P. A.; Rohrer, G. S. *Chem. Commun.* **2012**, *48*, 2012−2014.

(40) Li, L.; Rohrer, G. S.; Salvador, P. A. *J. Am. Ceram. Soc.* **2012**, *95*, 1414−1420.

(41) Li, S.; Lin, Y. H.; Zhang, B. P.; Nan, C. W.; Wang, Y. *J. Appl. Phys.* **2009**, *105*, 056105.

(42) Parida, K. M.; Reddy, K. H.; Martha, S.; Das, D. P.; Biswal, N. *Int. J. Hydrogen Energy* **2010**, *35*, 12161−12168.

(43) Chan, C. K.; Porter, J. F.; Li, Y. G.; Guo, W.; Chan, C. M. *J. Am. Ceram. Soc.* **1999**, *82*, 566−572.

(44) Baiju, K. V.; Shukla, S.; Sandhya, K. S.; James, J.; Warrier, K. G. K. *J. Phys. Chem. C* **2007**, *111*, 7612−7622.

(45) Luo, J. H.; Maggard, P. A. *Adv. Mater.* **2006**, *18*, 514−517.

(46) Wang, C.; Bottcher, C.; Bahnemann, D. W.; Dohrmann, J. K. *J. Mater. Chem.* **2003**, *13*, 2322−2329.

(47) Ginley, D. S.; Butler, M. A. *J. Appl. Phys.* **1977**, *48*, 2019−2021.

(48) Sunkara, S. S.; Pandey, R. K. *Ceram. Trans.* **1995**, *60*, 83−93.

(49) Blasse, G.; Dirksen, G. J.; Dekorte, P. H. M. *Mater. Res. Bull.* **1981**, *16*, 991−998.

(50) Wilson, N. C.; Muscat, J.; Mkhonto, D.; Ngoepe, P. E.; Harrison, N. M. *Phys. Rev. B* **2005**, *71*, 075202.

(51) Dai, Z.; Naramoto, H.; Narumi, K.; Yamamoto, S.; Miyashita, A. *J. Appl. Phys.* **1999**, *85*, 7433−7437.

(52) Carreon, M. A.; Choi, S. Y.; Mamak, M.; Chopra, N.; Ozin, G. A. *J. Mater. Chem.* **2007**, *17*, 82−89.

(53) Houas, A.; Lachheb, H.; Ksibi, M.; Elaloui, E.; Guillard, C.; Herrmann, J. M. *Appl. Catal. B* **2001**, *31*, 145−157.

(54) Wu, T.; Liu, G.; Zhao, J.; Hidaka, H.; Serpone, N. *J. Phys. Chem. B* **1999**, *103*, 4862−4867.

(55) Zhao, W.; Chen, C.; Li, X.; Zhao, J.; Hidaka, H.; Serpone, N. *J. Phys. Chem. B* **2002**, *106*, 5022−5028.

(56) Yamashita, H.; Harada, M.; Misaka, J.; Takeuchi, M.; Neppolian, B.; Anpo, M. *Catal. Today* **2003**, *84*, 191−196.

(57) Serpone, N.; Lawless, D.; Disdier, J.; Herrmann, J. M. *Langmuir* **1994**, *10*, 643−652.

(58) Nahar, M. S.; Hasegawa, K.; Kagaya, S. *Chemosphere* **2006**, *65*, 1976−1982.

(59) Wang, X. H.; Li, J. G.; Kamiyama, H.; Katada, M.; Ohashi, N.; Moriyoshi, Y.; Ishigaki, T. *J. Am. Chem. Soc.* **2005**, *127*, 10982−10990.

(60) Wang, Y. W.; Xu, H.; Wang, X. B.; Zhang, X.; Jia, H. M.; Zhang, L. Z.; Qiu, J. R. *J. Phys. Chem. B* **2006**, *110*, 13835−13840.

(61) Imanishi, A.; Tsuji, E.; Nakato, Y. *J. Phys. Chem. C* **2007**, *111*, 2128−2132.

(62) Butler, M. A.; Ginley, D. S. *J. Electrochem. Soc.* **1978**, *125*, 228−232.

(63) Yu, J.; Xiang, Q.; Zhou, M. *Appl. Catal. B* **2009**, *90*, 595−602.

(64) Goodenough, J. B.; Stickler, J. J. *Phys. Rev.* **1967**, *164*, 768−778.

(65) Fennie, C. J. *Phys. Rev. Lett.* **2008**, *100*, 167203.